

# Mosaic growth of GaN on (0001) sapphire: A high-resolution electron microscopy and crystallographic study of threading dislocations from low-angle to high-angle grain boundaries

V. Potin, P. Ruterana,\* and G. Nouet

*Laboratoire d'Etudes et de Recherche sur les Matériaux, UPRESA CNRS 6004, Institut des Sciences de la Matière et du Rayonnement, 6 Boulevard du Maréchal Juin, 14050 Caen Cedex, France*

R. C. Pond

*Department of Materials Science and Engineering, The University of Liverpool, Liverpool L69 3GH, England*

H. Morkoç

*Virginia Commonwealth University, Department of Electrical Engineering, Richmond, Virginia 23284-3072*

(Received 14 September 1999)

Using high-resolution electron microscopy, anisotropic elasticity calculations, and image simulations, typical contrast was identified for the  $\vec{a}$  pure edge threading dislocations in GaN layers grown by molecular-beam epitaxy on sapphire. Their atomic structure was found to exhibit 5/7, or 8 atom cycles. The two configurations were observed at a similar frequency for isolated dislocations and low-angle boundaries. Coincidence grain boundaries have been studied and they are all made of  $\vec{a}$  pure-edge dislocations with the above identified atomic structures. A topological analysis of high-angle boundaries has been carried out in order to determine the defect content at the interfaces. The defects introduced on deviation from coincidence are associated with steps and their Burgers vectors correspond to the smallest vectors of the displacement shift complete set. At the interfaces, defect free steps, which belong to the sides or diagonal of the coincident site lattice unit cell, have been found to occur. The reconstruction of some boundaries was only possible by taking into account the occurrence of structural units which exhibit 4-atom ring cycles for the dislocation cores. In nonsymmetric interfaces, a new structural unit made of 5/4/7 atom rings has been found to constitute the core of one grain boundary dislocation.

## I. INTRODUCTION

There is currently a tremendous research effort on the Ga-based III-V semiconductors nitrides due to their very promising application potential in optoelectronics and in high-power, high-frequency devices. Most of the results have been obtained in layers containing a huge density of threading dislocations following growth on sapphire.<sup>1</sup> The origin of this density has been suggested to be due to a peculiar growth mode, which was named “mosaic growth.”<sup>2</sup> Due to the large misfits, the adjacent islands are misoriented mainly by rotation about the  $c$  axis and their boundaries are made of  $\vec{a}$  pure-edge dislocations. In general, they can be also tilted and  $\vec{c}$  or  $\vec{a} + \vec{c}$  dislocations may be formed.<sup>3</sup> The above growth mode may explain misorientation of 0.5 to 2° between adjacent grains.<sup>2</sup> In practice, the growth of GaN on various substrates like sapphire may be rather complex and layers can contain many nanoscopic areas, which largely deviate from the usual epitaxial relationship.<sup>4,5</sup> They are usually located inside the buffer layer and their optimal size has been shown to lead to good quality epitaxial layers.<sup>6</sup>

The rather good optical properties have been tentatively explained by assuming that these dislocations could bear reconstructed core that did not exhibit states inside the band gap.<sup>7</sup> This reconstruction was confirmed by Z-contrast observation at atomic resolution.<sup>8</sup>

However, during the last few years, experimental results

have shown that these defects may be responsible for the yellow-band luminescence;<sup>9</sup> and it is now agreed that in order to have long-lived devices, it is necessary to drastically decrease their density. This has led to such growth methods as epitaxial lateral overgrowth from which densities close to  $10^7 \text{ cm}^{-2}$  have been reached.<sup>10,11</sup> In such samples, areas without dislocations can be a few microns across with a perfect correlation to the yellow-band emission.<sup>12</sup> Therefore, this emission may originate either from geometrical and relaxation effects which are dependent on the core structure of the defect, or from the impurities that may be pinned in these dislocations and this has not yet been cleared out.

It was our aim to carry out a detailed analysis of the core structure of these dislocations in order to assess their atomic structure. Moreover, in the studied molecular-beam epitaxy GaN layers, high-angle grain boundaries were found to form and it was of interest to investigate their atomic structure. As they are also formed by rotation about the  $c$  axis, they are made of  $\vec{a}$  pure-edge dislocations. In former studies of grain boundaries, it has been pointed out that particular structural units of dislocation cores may form coincident grain boundaries,<sup>13,14</sup> which are crystallographically favoured<sup>15</sup> and low-energy configurations.<sup>16</sup>

More recent studies tend to show that three-dimensional coincidence structures are only approximations,<sup>17</sup> moreover, theoretical work has demonstrated that structural units may only be valid for pure tilt or pure twist grain boundaries.<sup>18</sup> In lower symmetry materials, the constrained coincidence site

lattice formalism introduces artificial long-range strains and is not adequate for the study of interfacial defects.<sup>17</sup> More accurate attempts have been made in the last years in order to formalize the understanding of interfacial defects.<sup>19,20</sup> The most extensive one has been developed by Pond and Vlachavas;<sup>20</sup> it uses the whole symmetry of the two crystals that are abutted at the interface in order to determine *a priori* the interfacial defect content. Moreover, an experimental analysis of high-resolution micrographs using circuit mapping, which is a generalization of the Burgers circuit, allows to determine the character of the interfacial defects. The combination of the theoretical and experimental analysis of the micrographs constitute the topological investigation of interfacial defects,<sup>21</sup> it will be commented on and then used in order to interpret our observations.

In this paper, the atomic structure of  $\vec{a}$  pure-edge dislocations contained in low- and high-angle boundaries has been investigated. In case of deviation from coincidence, the interfacial defects present in the high-angle grain boundaries were analyzed using the topological theory. The analyzed GaN layers contained densities of threading dislocations in the low  $10^{10} \text{ cm}^{-2}$ . The high-angle boundaries were observed in some specimens although no change had been made in the growth conditions. Such grains could be as large as 1 micron across, which is smaller than the low-angle grains, which extend to tens of microns.

## II. CRYSTALLOGRAPHIC CONSIDERATIONS

Grain boundary structures can often be described conveniently in terms of an array of line-defects superimposed on some singular configuration.<sup>21</sup> The function of the defect array is to accommodate small angular deviations from the special misorientation of the singular case. Although there is no simple correlation between geometric parameters and interfacial free energy, considerable evidence has been found showing that two-dimensionally periodic boundaries are sometimes favorable.<sup>22</sup> There is also some evidence that other one-dimensionally periodic structures are singular, for example certain boundaries in ZnO.<sup>23</sup> In the present paper, it is helpful to identify misorientations corresponding to potentially singular values. Since the GaN films studied here grow with their basal plane parallel to the  $\text{Al}_2\text{O}_3$  substrate, the most common type of misorientation encountered is relative rotation of one crystal with respect to an adjacent one about their common  $[0001]$  axis. Thus, we shall concentrate here on the nature of singular configurations that can arise from such misorientations. This can be done using the method developed by Pond and Vlachavas,<sup>19</sup> which identifies the symmetry of dichromatic patterns and complexes. However, before this issue is discussed, it is necessary to consider briefly the crystallography of single crystals of GaN.

The structure of a unit cell of GaN projected along  $[0001]$  is depicted schematically in Fig. 1. The open and filled symbols represent Ga sites at heights  $+\frac{1}{4}c$ , respectively, and for simplicity the  $N$  sites are not shown. These latter sites would be at heights  $3/8c$  above or below each Ga sites depending on the crystal's polarity. Note that the origin chosen in Fig. 1 is at height zero on the axis of a "tunnel" between the atomic columns. This point is a convenient origin for definition of the crystal-symmetry operations. Using the no-

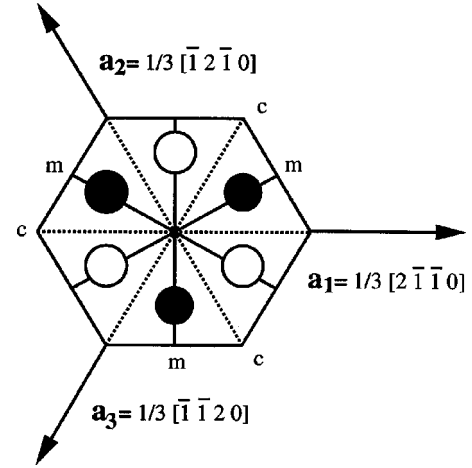


FIG. 1. Schematic representation of the unit cell of GaN, viewed along  $[0001]$ ; only the Ga sublattice has been drawn, open and filled circles are related by a glide symmetry operation.

tation of the International Tables for Crystallography,<sup>24</sup> the twelve operations (excluding the infinite set of translations) in the crystal's space group,  $P6_3mc$ , are listed in Table I.

The polarity of the crystal cannot be established on micrographs viewed along  $[0001]$ , although other methods can be used to determine it.<sup>25</sup> Crystallographically, inversion related crystals are interrelated by the twelve operations obtained by decomposing the parent group  $P6_3/mmc$  with respect to  $P6_3mc$ . The parent symmetry would be exhibited by the imaginary structure comprising filled Ga sites as depicted in Fig. 1 in addition to both types of  $N$  sites referred to above being filled. The origin chosen in this work corresponds to the location of the center of symmetry in the parent structure. We note that some symmetry operations which interrelate "up" and "down" polarity variants do not pass through the chosen origin, for example the mirror plane parallel to  $(0001)$  in the parent group  $P6_3/mmc$ .

We now consider the symmetry of dichromatic complexes, i.e., configurations that can be visualized by allowing two crystal structures relatively rotated about  $[0001]$  to inter-

TABLE I. The twelve symmetry operations of the  $P6_3mc$  space group of GaN, along with their location and glide or screw component.

Numbering	Symmetry operation	Location	Glide or screw component
1	1		
2	3+	0,0,0,z	
3	3-	0,0,0,z	
4	2	0,0,0,z	0,0,0,1/2
5	6-	0,0,0,z	0,0,0,1/2
6	6+	0,0,0,z	0,0,0,1/2
7	<i>m</i>	$x, -x, 0, z$	
8	<i>m</i>	$x, 2x, -3x, z$	
9	<i>m</i>	$2x, x, -3x, z$	
10	<i>c</i>	$x, x, -2x, z$	0,0,0,1/2
11	<i>c</i>	$x, 0, -x, z$	0,0,0,1/2
12	<i>c</i>	$0, y, -y, z$	0,0,0,1/2

penetrate. The configuration created by two lattices rather than two crystals is called dichromatic pattern.<sup>19</sup> One crystal is designated white ( $\lambda$ ), and the other black ( $\mu$ ). The symmetry operations exhibited by these crystals,  $\mathcal{W}(\lambda)_i$ , with  $i = 1 \rightarrow 12$ , and similarly  $\mathcal{W}(\mu)_j$  are listed in Table I (excluding translations). The relative orientation is defined by the operation  $\mathcal{P} = (P, \mathbf{p})$  which transforms white vectors into corresponding black ones (expressed in the white coordinate frame).  $P$  may either be a rotation about [0001], thereby relating crystals of the same polarity, or a rotoinversion relating crystals of opposite polarity. The translation  $\mathbf{p}$  represents the shift of the black crystal origin following the operation  $P$ . This formalism enables the symmetry of dichromatic complexes to be established for any relative orientation and position of the  $\lambda$  and  $\mu$  crystals. Coincident symmetry operations in such complexes arise when black and white crystal symmetry operations coincide and correspond to the intersection of the crystal space groups, i.e.,  $\Phi(\lambda) \cap \Phi(\mu)$ . Explicitly, the coincident operations in the complex,  $\mathcal{W}(c)$ , are the solutions to the following identity:<sup>26</sup>

$$\mathcal{W}(\lambda)_j = \mathcal{P}\mathcal{W}(\mu)_i\mathcal{P}^{-1} = \mathcal{W}(c)_k. \quad (1)$$

This set will include an infinite number of translations parallel to [0001] for all rotations, and a three-dimensional set also known as the coincident site lattice (CSL) for special misorientations, independent of any translation  $\mathbf{p}$ . Other coincident operations arising for any value of rotation about [0001] may be broken by translation  $\mathbf{p}$ . In addition, color reversing or antioperations, which relate black features to white and vice versa, will also arise. These can be identified by inspection of the multiplicity of equivalent descriptions of  $\mathcal{P}$ , i.e.,  $\mathcal{P}\mathcal{W}(\lambda)_i$ . Those operations in this set that have the form of symmetry operations are antioperations in the space group of the complex,  $\mathcal{W}(c)_k$ , i.e.,

$$\mathcal{P}\mathcal{W}(\lambda)_j = \mathcal{W}'(c)_k. \quad (2)$$

The space group of a dichromatic complex is then given by the union of the coincident group and the set  $\mathcal{W}'(c)_k$ .<sup>26</sup> These issues are illustrated further below.

In the present paper, grain boundaries with rotations close to the following special values have been observed (13.17°, 21.79°, 17.90°), the corresponding coincident site densities are  $\Sigma = 19, 7, 31$ , respectively. The matrices,  $P$ , corresponding to these rotations are listed in the appendix. These  $4 \times 4$  matrices act on 4 vectors as introduced by Frank<sup>27</sup> and applied to interface problems by Pond *et al.*<sup>28</sup> We note that the CSL's resulting from rotations  $\theta$  and  $\theta \pm 60^\circ$  are identical because the lattices of the  $\lambda$  and  $\mu$  crystals exhibit the symmorphic symmetry  $P6/m\,mm$  which includes a sixfold rotation axis parallel to [0001].

For rotations about [0001] there are six solutions to expression (1) as listed in Table II for the case where  $\mathbf{p} = 0$ ; these solutions are independent of  $\theta$ . Similarly, six antioperations are solutions to expression (2) independent of  $\theta$ , as listed in Table II. Thus, the space groups of dichromatic complexes for rotations about [0001] are always  $p6_3m'c'$  except when three dimensional (3D) CSL's arise; the symmetry becoming then  $P6_3m'c'$ . An illustration of the  $\Sigma = 7$  dichromatic complex is given in Fig. 2(a). We note that complementary complexes, i.e., for rotations  $\theta$  and  $60^\circ - \theta$ ,

TABLE II. The twelve symmetry operations of the dichromatic pattern  $p6_3m'c'$  representing two GaN crystals rotated about [0001].

Coincident operations			
Numbering	Symmetry operation	Location	Glide or screw component
1	1		
2	3+	0,0,0,z	
3	3-	0,0,0,z	
4	2	0,0,0,z	0,0,0,1/2
5	6-	0,0,0,z	0,0,0,1/2
6	6+	0,0,0,z	0,0,0,1/2
Antioptions			
Numbering	Symmetry operation	Location	Glide or screw component
1	$m'$	$x, -x, 0, z$	
2	$m'$	$x, 2x, -3x, z$	
3	$m'$	$2x, x, -3x, z$	
4	$c'$	$x, x, -2x, z$	0,0,0,1/2
5	$c'$	$x, 0, -x, z$	0,0,0,1/2
6	$c'$	$0, y, -y, z$	0,0,0,1/2

could be allocated the space groups  $P6_3m'c'$  and  $P6_3c'm'$  by appropriate choice of unit cells, as illustrated in Figs. 2(a) and 2(b). In other words, the two complexes differ only in the position of their  $c'$  and  $m'$  planes. We also note that complementary complexes arise for the same rotation  $\theta$ , but with  $\mathbf{p} = 0$  in one case and  $\mathbf{p} = 1/2c$  in the other. Similarly, they also arise for roto and rotoinversion operations,  $\theta$  and  $\bar{\theta}$ . Finally, we note that a special case arises for the  $60^\circ$  rotoinversion operation; in this instance the space group becomes  $P6'/m'mm$  with  $\Sigma = 1$ , i.e., inversion related crystals rotated relatively by  $60^\circ$  around [0001].

Interfacial defects arise when the black and white crystal surfaces abutting at an interface are not complementary and exhibit incompatible steps.<sup>29</sup> Following the topological theory of line defects in interfaces,<sup>26</sup> the Burgers vectors  $\mathbf{b}_{ij}$  of the admissible interfacial dislocations are given by

$$\mathbf{b}_{ij} = \mathbf{t}(\lambda)_j - P\mathbf{t}(\mu)_i, \quad (3)$$

where  $\mathbf{t}(\lambda)_j$  and  $\mathbf{t}(\mu)_i$  represent the  $j$ th and  $i$ th translations in the  $\lambda$  and  $\mu$  crystals, respectively and  $P$  is a matrix that re-expresses  $\mathbf{t}(\mu)_i$  in the  $\lambda$  coordinate frame. Thus,  $\mathbf{b}_{ij}$  is the difference between the two translations expressed in the same coordinate frame. Moreover, the vectors  $\mathbf{b}_{ij}$  are vectors joining white to black sites in the dichromatic pattern. Those with the smallest magnitudes are oriented parallel to the sides of the unit cells of the dichromatic patterns.

The cores of such interfacial defects are associated with steps. The heights of the free surface steps are given by  $h(\lambda)_j = \mathbf{n}_\lambda \cdot \mathbf{t}(\lambda)_j$  and  $h(\mu)_i = P^{-1}\mathbf{n}_\lambda \cdot \mathbf{t}(\mu)_i = \mathbf{n}_\mu \cdot \mathbf{t}(\mu)_i$ ,  $\mathbf{n}$  is the unit vector normal to the interface, it is oriented towards the  $\lambda$  crystal. These heights are quantified in units of  $d_{(hkl)}$ , the interplanar spacing of the lattice planes parallel to the interface in the  $\lambda$  and  $\mu$  crystals.

The interfacial defects observed using high-resolution electron microscopy (HREM) can be characterized by circuit mapping as proposed by Pond.<sup>21</sup> In this procedure, a circuit

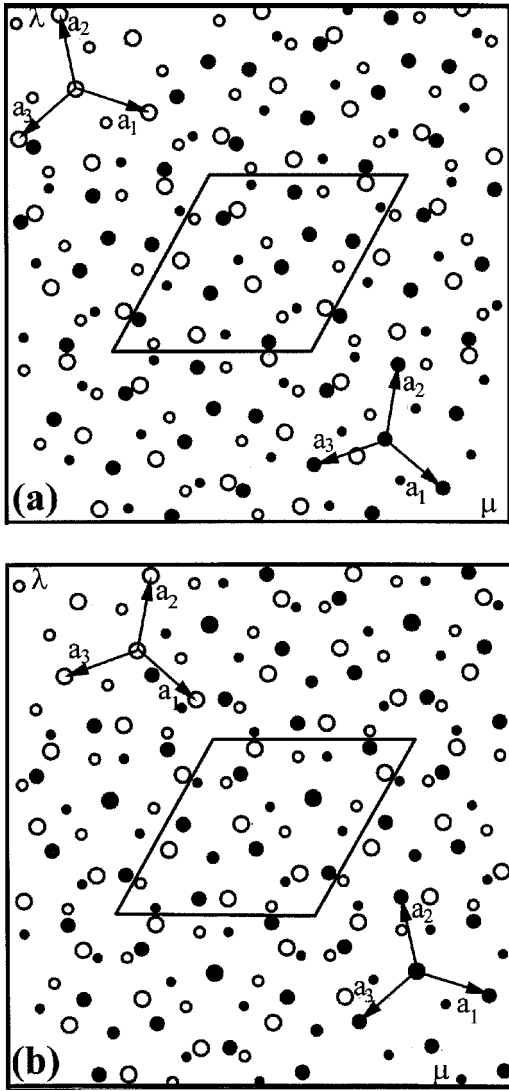


FIG. 2. Dichromatic complexes of  $\Sigma=7$ , ( $\theta=21.79^\circ/[0001]$ ) the open and filled circles represent  $\lambda$  and  $\mu$ , respectively. The large and small circles are related by a  $c/2$  height. The space groups of the unit cell are (a)  $P6_3m'c'(\theta)$  and (b)  $P6_3c'm'(60^\circ-\theta)$ .

is constructed around an interfacial defect on the micrograph, with segments in the  $\lambda$  and  $\mu$  crystals connected by displacements  $\mathbf{p}_1$  and  $\mathbf{p}_2$  across the interface. These circuit segments are designated by  $C(\lambda)$  and  $C(\mu)$  and the complete circuit  $C(\lambda, \mu)$ , as expressed in the  $\lambda$  coordinate frame, is given by

$$C(\lambda, \mu) = (I, \mathbf{p}_2)^{-1} P C(\mu) P^{-1} (I, \mathbf{p}_1) C(\lambda). \quad (4)$$

In the simplest cases, the translations  $\mathbf{p}_1$  and  $\mathbf{p}_2$  are of opposite sign, so their contribution to the total circuit cancels. When the circuit is mapped into a reference space, any closure failure is equal to the total defect content. Using the RH/FS convention, the defect is given by  $C(\lambda, \mu)^{-1}$ , where  $C(\lambda, \mu)$  represents the irreducible expression of the closure failure. For circuits constructed using translation operations,  $C(\lambda) = [I, \mathbf{c}(\lambda)]$ ,  $C(\mu) = [I, \mathbf{c}(\mu)]$ , and  $P = (P, \mathbf{p})$ , we obtain

$$\begin{aligned} C(\lambda, \mu)^{-1} &= [I, -\mathbf{c}(\lambda)](P, \mathbf{p})[I, -\mathbf{c}(\mu)](P^{-1}, -P^{-1}\mathbf{p}) \\ &= [I, -\mathbf{c}(\lambda) - P\mathbf{c}(\mu)], \text{ for } \mathbf{p} = 0. \end{aligned}$$

Thus,

$$\mathbf{b}_{ij} = -\mathbf{c}(\lambda, \mu) = -\mathbf{c}(\lambda) - P\mathbf{c}(\mu). \quad (5)$$

Moreover, the step heights can be determined experimentally from the above circuit and  $h(\lambda)_j = -\mathbf{n}_\lambda \cdot \mathbf{c}(\lambda) / d_{(hkl)j}$  whereas  $h(\mu)_i = P^{-1}\mathbf{n}_\lambda \cdot \mathbf{c}(\mu) / d_{(hkl)i} = \mathbf{n}_\mu \cdot \mathbf{c}(\mu) / d_{(hkl)i}$ . As shown by Braisaz *et al.*,<sup>30</sup> an interfacial dislocation is uniquely described by its associated step height in the  $\lambda$  and  $\mu$  crystals.<sup>31,32</sup> Therefore, in the following, we use the notation proposed by Braisaz *et al.*<sup>30</sup> to write Burgers vectors as  $\mathbf{b}_{p/q}$  where  $p$  and  $q$  are defined as  $h(\lambda)_j = p d_{(hkl)j}$  and  $h(\mu)_i = q d_{(hkl)i}$ . In theory, a multiplicity of step configurations can arise for a defect with particular  $\mathbf{b}$  because translation vectors of the dichromatic pattern can be added to both  $\mathbf{t}(\lambda)_j$  and  $\mathbf{t}(\mu)_i$  without modifying  $\mathbf{b}$ . Therefore, in order to describe unambiguously the observed defect, it is necessary to determine the associated values of  $\mathbf{t}(\lambda)_j$  and  $\mathbf{t}(\mu)_i$  characterising the step.

This treatment is more general than the formalism proposed by Bollmann,<sup>15</sup> which only took into account translation operators in the analysis of interfacial defects. In fact, it is now possible to determine all types of defects, because they can be directly related to the symmetry elements which are broken at a particular interface. Obviously, the different classes of interfacial defects have already been identified. In our case, the defects that are expected in the grain boundaries between crystallites that are rotated about the  $[0001]$  axis are of class 1, i.e., broken translation symmetry. Therefore, their Burgers vectors as determined in the dichromatic patterns are identical to those of the displacement shift complete<sup>15</sup> set (DSC).

### III. EXPERIMENTAL DETAILS

The GaN layers were grown on the (0001) sapphire surface by  $\text{NH}_3$  gas source molecular-beam epitaxy. The deposition was performed at  $800^\circ\text{C}$  on a low-temperature GaN buffer layer ( $550^\circ\text{C}$ , 40 nm thickness), and the active layer thickness varied from one specimen to the other between one and two microns.

The transmission electron microscopy samples were thinned down to  $100 \mu\text{m}$  by mechanical grinding and dimpled down to  $10 \mu\text{m}$ . Electron transparency was obtained by ion milling at 5 kV with a liquid  $\text{N}_2$  cold stage. A final step at 3 kV was used to decrease ion-beam damage. HREM experiments were carried out along the  $[0001]$  zone axis on a Topcon 002B electron microscope operating at 200 kV with a point to point resolution of 0.18 nm ( $C_s = 0.4 \text{ mm}$ ). Models of the  $1/3 \langle 11\bar{2}0 \rangle$  dislocation were generated using anisotropic elasticity theory.<sup>33</sup> The simulation of the experimental images was possible by the use of the electron microscopy software.<sup>34</sup>

### IV. THE ATOMIC STRUCTURE OF THE EDGE DISLOCATIONS

In most GaN layers, transmission electron microscopy studies have clearly shown that the threading dislocations form low-angle boundaries, which are misoriented by a few degrees,<sup>2,3</sup> although some may be randomly distributed.<sup>35</sup>

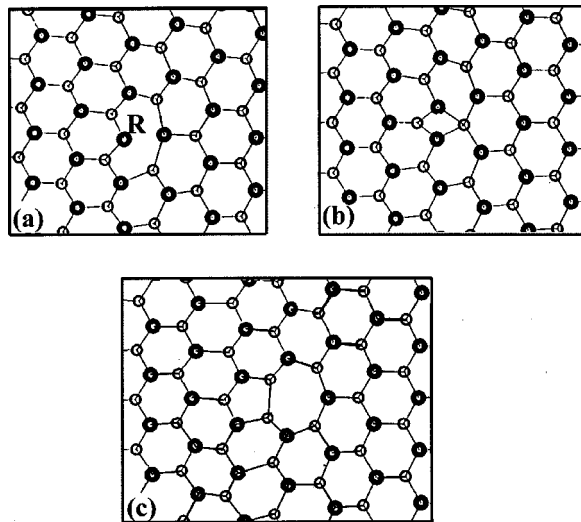


FIG. 3. Anisotropic elasticity models for the core structure of the  $\vec{a}$  edge threading dislocation viewed along [0001]: (a) 8, (b) 4, (c) 5/7 atom cycles.

The majority of the crystal dislocations were reported to have pure-edge character, with Burgers vectors of  $1/3 \langle 11\bar{2}0 \rangle$ , even if  $\mathbf{c}$  and  $\mathbf{a}+\mathbf{c}$  ones are present as well.<sup>36</sup> Their origin was shown to be the mosaic growth mode, which leads to GaN layers made of individual islands. If the islands are slightly rotated around the  $c$  axis,  $\vec{a}$  pure-edge dislocations formed at their coalescence whereas the  $\mathbf{c}$  and  $\mathbf{a}+\mathbf{c}$  ones may be due to small tilts of the  $c$  axis.<sup>2</sup>

In the wurtzite structure, when seen along the  $\mathbf{c}$  axis, the  $\vec{a}$  pure-edge dislocation may have one of the six equivalent  $1/3 \langle 11\bar{2}0 \rangle$  Burgers vectors. Therefore, we have used these six possibilities in anisotropic elasticity calculations in order to generate the possible atomic configurations of the dislocation. Although the elasticity calculations present a singular point in the core of a dislocation, we have kept the generated configurations for comparison with the experimental observations, as far as the distances between nearest-neighbor atoms inside the core were not too far from the usual ones in GaN. Actually, only two possible structures are obtained for the core: 8 and 4 atom rings as shown on Figs. 3(a) and 3(b). In contrast to the 4 configuration, the 8-atom cycle may have a dangling bond inside its core. The two models differ only by the position of atom  $R$  as shown in Fig. 3(a). However it cannot be exactly calculated in the anisotropic elasticity formalism, which is only valid at distances larger than the Burgers vector from the core. By deleting that atom, it was possible to construct a configuration with 5/7 atom rings [Fig. 3(c)], which either does not exhibit any dangling bond.

For isolated or very low-angle boundaries ( $<1^\circ$ ) two typical images were obtained corresponding to the two first maxima of contrast for our microscope (defocus windows:  $-20$  to  $-32$  and  $-50$  to  $-60$  nm). The estimated thickness is close to 14 nm whereas the defocus values are around  $-26$  and  $-54$  nm [Figs. 4(a) and 4(b)], [Figs. 4(c) and 4(d)], respectively.

We have then carried out systematic image simulations using the above models. Figure 5 shows the results for the two defocus windows, the sample thickness is 14 nm. These

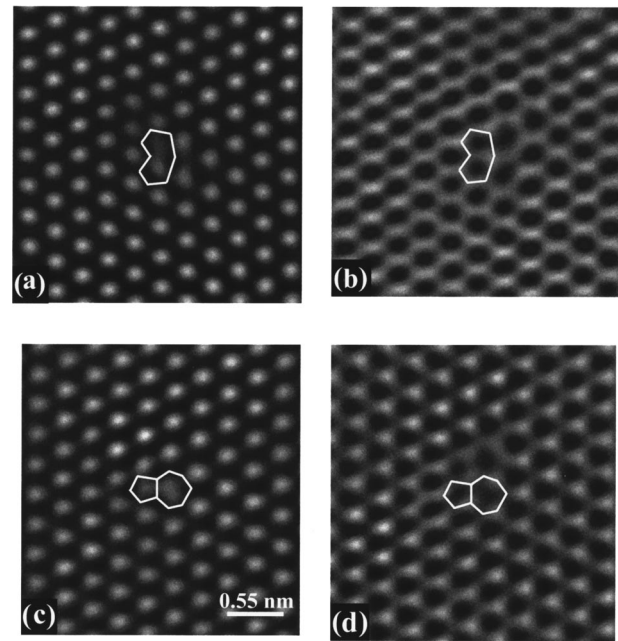


FIG. 4. Two typical images exhibited by the isolated dislocations, at  $-26$  and  $-54$  nm defocus in areas of thickness close to 14 nm, atom cycles have been superimposed: (a) and (b) 8 atom rings; (c) and (d) 5/7 atom rings.

images reproduce the contrast observed in the experimental micrographs for the isolated dislocations: Figs. 5(a) and 5(b) correspond to the 8 atom rings of Figs. 4(a) and 4(b); whereas the 5/7 atom rings of Figs. 5(e) and 5(f) agrees with the contrast of Figs. 4(c) and 4(d). During these experiments, the two configurations were seen at similar frequency and in these isolated dislocations, no other configuration was observed.

These two configurations of the dislocations can be compared to the geometrical models discussed by Hornstra for the Lomer dislocation in the diamond lattice.<sup>37</sup> Observations of Lomer dislocations in diamond cubic/zinc blende materials Si, Ge,<sup>38</sup> and at the GaAs/Si (Ref. 39) indicate that their atomic configurations are either 5/7 or 8 atom rings.

## V. THE PURE TILT GRAIN BOUNDARIES

Among twist and tilt high-angle grain boundaries observed, we have focused our attention on those that are rotated around the  $c$  axis. It appears that the values of the rotation angle are very close to those of  $\Sigma$  boundaries in the coincidence site lattice notation (CSL). These boundaries are  $\Sigma = 7(21.79^\circ)$ ,  $\Sigma = 19(13.17^\circ)$ , and  $\Sigma = 31(17.90^\circ)$ .

### A. The $\Sigma = 19$ boundary

The analyzed grain had a regular shape with four straight boundaries linked together by angles of  $60^\circ$  or  $120^\circ$ , its size is about  $60 \times 50 \text{ nm}^2$ . The value of the rotation angle was measured on the corresponding diffraction pattern as  $13.2^\circ \pm 0.2^\circ$  close to that of  $\Sigma = 19$  ( $\theta = 13.17^\circ$ ) in the CSL notation. The corresponding dichromatic pattern is shown in Fig. 6, and it results from the interpenetration of two lattices designated as white ( $\lambda$ ) and black ( $\mu$ ). The two lattices are rotated around their common sixfold axis. For this dichromatic

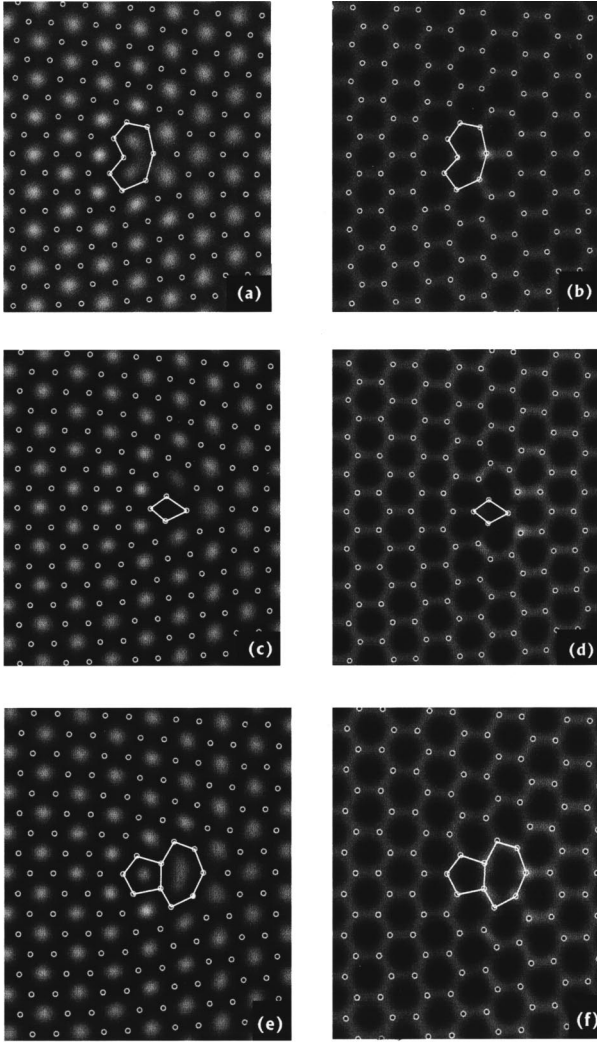


FIG. 5. Simulated images using the 8, 4, and 5/7 atom rings models: (a) and (b) correspond to 26 and  $-54$  nm defocus at a 14 nm thickness for the 8 atom rings; (c) and (d) represent the 4 atoms core configuration, (e) and (f) represent the 5/7 model.

pattern, a CSL unit cell has been constructed and its basis vectors are  $1/3 [71\bar{8}0]$ ,  $1/3 [\bar{1}8\bar{7}0]$ , and  $[0001]$  when expressed in the  $\lambda$  frame.

A part of the boundary is shown in Fig. 7, the white spots correspond to the tunnels at a defocus value close to  $-26$  nm. By comparison with the dichromatic pattern, the interface plane was found to be along a side of the CSL unit cell. On Fig. 7(a), the SXF circuit was drawn with  $\mathbf{c}(\lambda) = \mathbf{SX} = -6\vec{a}_1 + 9\vec{a}_3 = 1/3 [\bar{2}1\bar{3}240]_\lambda$  and  $\mathbf{c}(\mu) = \mathbf{XF} = 9\vec{a}_1 - 6\vec{a}_3 = 1/3 [24\bar{3}\bar{2}10]_\mu$ , corresponding to three periods of the CSL (indicated by the large black dots). The normal to the interface was determined by making the cross product of  $\mathbf{c}(\lambda)$  by  $[0001]$  and  $[0001]$  by  $\mathbf{c}(\mu)$  leading to  $\mathbf{n}_\lambda = [\bar{3}5\bar{2}0]_\lambda$  and  $\mathbf{n}_\mu = [\bar{2}5\bar{3}0]_\mu$ , respectively. For these three periods of the interface, the interface plane is along  $(\bar{3}5\bar{2}0)_\lambda / (\bar{2}5\bar{3}0)_\mu$  and it corresponds to a side of the CSL unit cell of  $\Sigma = 19$ .

If the circuit SVF corresponding to one period {i.e.,  $\mathbf{c}(\lambda) = \mathbf{SV} = 1/3 [\bar{7}\bar{1}80]_\lambda$  and  $\mathbf{c}(\mu) = \mathbf{VF} = 1/3 [8\bar{1}\bar{7}0]_\mu$ } is

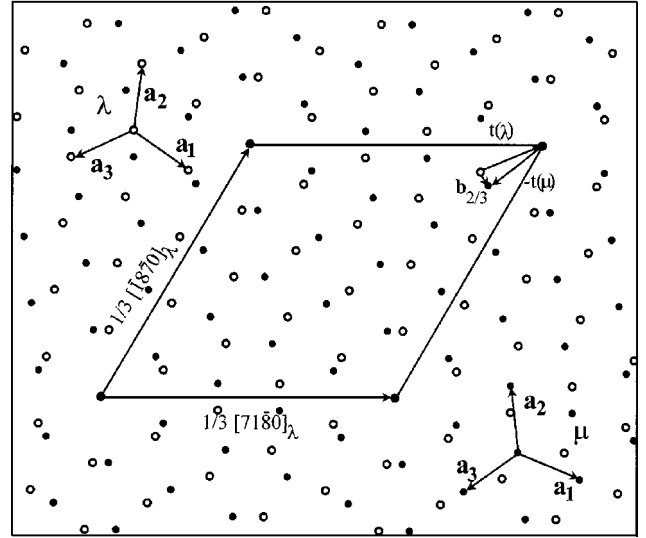


FIG. 6. Dichromatic pattern corresponding to  $\Sigma = 19$  in the CSL notation ( $13.17^\circ/[0001]$ ), the unit cell of the CSL has been drawn, parts of the  $\lambda$  and  $\mu$  crystals are shown. The smallest translation vectors  $\mathbf{t}(\lambda)$  and  $\mathbf{t}(\mu)$  and the corresponding Burgers vectors  $\mathbf{b}_{p/q}$  are drawn.

reported in the  $\lambda$  crystal, the closure failure **FS** is equal to  $1/3 [\bar{1}2\bar{1}0]$ . Thus, the primary dislocation for one period corresponds to the crystal dislocation  $\mathbf{b} = \vec{a}_2$ . If a circuit is mapped into the dichromatic pattern rather than into the lattice of a single crystal, secondary dislocations can be determined. In the previous case, this leads to  $\mathbf{c}(\lambda, \mu) = \mathbf{c}(\lambda) + P_{19}\mathbf{c}(\mu) = 0$  where  $P_{19}$  is given in the appendix. Therefore, in this part, the interface appears to be completely periodic without any additional defect.

However, such defects have been detected in this boundary. For example, the area designated by *YSZ* in Fig. 7(a) is characterized by  $\mathbf{c}(\lambda) = \mathbf{YS} = 1/3 [\bar{8}2\bar{1}00]_\lambda$  and  $\mathbf{c}(\mu) = \mathbf{SZ} = 1/3 [90\bar{9}0]_\mu = [30\bar{3}0]_\mu$ . After calculation, we obtained:  $\mathbf{c}(\lambda, \mu) = \mathbf{c}(\lambda) + P_{19}\mathbf{c}(\mu) = 1/57 [\bar{8}7\bar{1}0]_\lambda$ . By definition, the Burgers vector of this defect is the opposite of  $\mathbf{c}(\lambda, \mu)$  and is equal to  $1/57 [8\bar{7}\bar{1}0]_\lambda$ . This vector corresponds to an interfacial edge dislocation with the smallest magnitude in the dichromatic pattern and its angle with the interface plane is  $60^\circ$  as shown in the dichromatic pattern of Fig. 6.

The step height is  $h(\lambda)_j = -\mathbf{n}_\lambda \cdot \mathbf{c}(\lambda) / d(\bar{3}5\bar{2}0) = 2$  and  $h(\mu)_i = \mathbf{n}_\mu \cdot \mathbf{c}(\mu) = 3/d(\bar{2}5\bar{3}0)$ , leading to a  $\mathbf{b}_{2/3}$  interface dislocation.<sup>30,31</sup> Six similar secondary dislocations were identified in this boundary, they were spaced by eight periods of the CSL. Therefore, the deviation is  $0.19^\circ$  from the exact misorientation ( $\theta = 13.17^\circ$ ). These steps relate equivalent surfaces in the  $\lambda$  and  $\mu$  crystals by translations  $\mathbf{t}(\lambda)$  and  $\mathbf{t}(\mu)$  whose difference is equal to the Burgers vector of the secondary dislocation. In order to characterize completely the defect, it is necessary to determine the value of these translations. In theory, a multiplicity of configurations is possible and only a comparison with the experimental image would allow determining the exact configuration of the defect. For Burgers vector  $\mathbf{b}_{2/3} = 1/57 [8\bar{7}\bar{1}0]_\lambda$ , the associ-

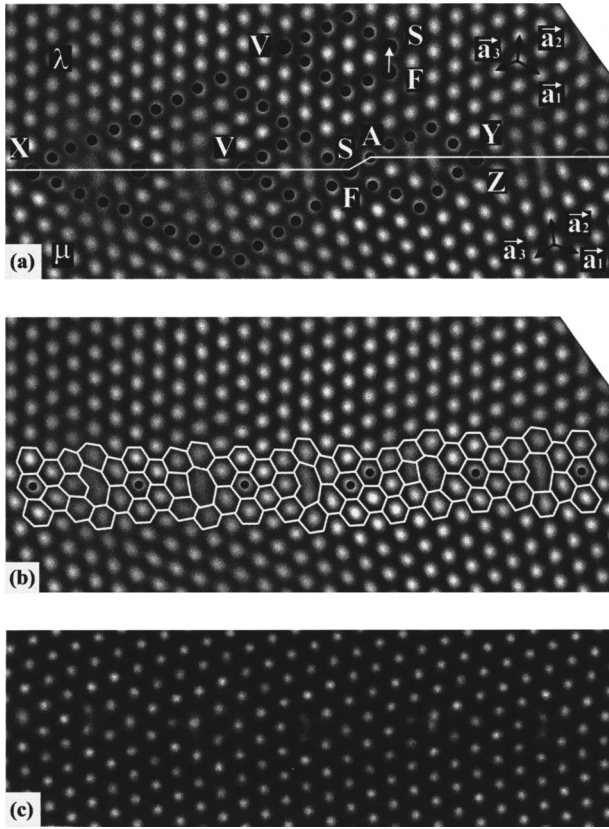


FIG. 7. High-resolution image of the  $\Sigma=19$  boundary: (a) Several circuits have been drawn. The large black dots define the periods of the  $\Sigma=19$  boundary. (b) Reconstruction of the boundary using edge dislocation cores. (c) Simulated image (thickness: 13 nm and defocus:  $-26$  nm).

ated smallest translation vectors are  $\mathbf{t}(\lambda) = 1/3 [11\bar{2}0]_{\lambda}$  and  $\mathbf{t}(\mu) = 1/3 [11\bar{2}0]_{\mu}$ . The steps heights are  $h(\lambda) = \mathbf{n}_{\lambda} \cdot \mathbf{t}(\lambda) = 2$ ,  $h(\mu) = \mathbf{n}_{\mu} \cdot \mathbf{t}(\mu) = 3$  and  $\mathbf{t}(\lambda) + P_{19}\mathbf{t}(\mu) = 1/57 [8\bar{7}\bar{1}0]_{\lambda}$ . Moreover, these values are consistent with the experimental image [Fig. 7(a)].

In order to reconstruct the core of the primary dislocations, we have used some configurations which had been generated for the study of  $\vec{a}$  pure-edge dislocations. A careful examination of the boundary shows that different contrasts are exhibited by the primary dislocations. For example, as shown in Fig. 7(a), between V and S, the core of the dislocation exhibits a 8-atom ring whereas between S and Y, it is a 5/7 one. Similarly, the whole boundary has been reconstructed and it appears that it is made only of 8- and 5/7-atom rings. In the experimental image [Fig. 7(b)], the sequences of 5/7- and 8-atom rings are shown and a good agreement is observed with the simulated image (thickness = 13 nm, defocus =  $-26$  nm) based on this reconstruction [Fig. 7(c)].

This example of a symmetric grain boundary which exhibits a small deviation from the  $\Sigma=19$  exact misorientation does not show special features for the  $\vec{a}$  dislocation cores, their atomic structure is identical to that of the above determined for the isolated dislocations.

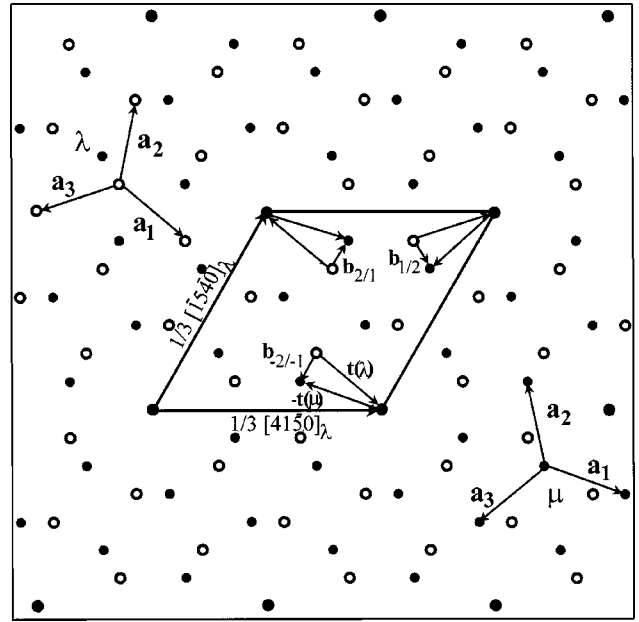


FIG. 8. Dichromatic pattern corresponding to  $\Sigma=7$  ( $21.79^\circ/[0001]$ ), the unit cell of the CSL has been drawn. The smallest translation vectors  $\mathbf{t}(\lambda)$  and  $\mathbf{t}(\mu)$  and the corresponding Burgers vectors  $\mathbf{b}_{p/q}$  are shown.

### B. The $\Sigma=7$ symmetric boundary

Unlike the  $\Sigma=19$  grain, which was made of straight boundaries, this grain is very irregular. Its boundaries mean-der in the matrix and the grain is crossed by  $\{11\bar{2}0\}$  stacking faults previously characterized.<sup>40,41</sup> Moreover, the boundaries are sometimes decorated with small voids. In the following, we discuss the results obtained on the straight areas of the boundary. Diffraction analysis indicates a rotation angle equal to  $22^\circ \pm 0.2^\circ$ , close to that of  $\Sigma=7$  in the CSL notation ( $\theta=21.79^\circ$ ).

In the dichromatic pattern corresponding to  $\Sigma=7$  (Fig. 8), a CSL unit cell is drawn with its  $1/3 \langle 41\bar{5}0 \rangle$  sides. The orientation of the experimental image according to the dichromatic pattern indicates that the boundary is along a side of the unit cell. This is confirmed by studying the circuit SXF for one period in the  $\lambda$  and  $\mu$  frames [Fig. 9(a)]. The details are given in Table III and the indices of the interface plane are  $(\bar{2}3\bar{1}0)_{\lambda}/(\bar{1}3\bar{2}0)_{\mu}$ . This circuit has been reported in the  $\lambda$  lattice and the Burgers vector was found to correspond to one dislocation core  $\vec{a}_2$ .

This grain boundary has been reconstructed and the cores of the primary dislocations exhibit 8- and 5/7-atom rings. Whereas for  $\Sigma=19$  boundary, the two configurations were alternated, for this  $\Sigma=7$  boundary, we observed five 5/7 configurations followed by two 8-atom ring ones. A simulated image of this boundary was carried out based on the reconstruction indicated on the experimental image and a good agreement was obtained for a thickness of 8 nm and a defocus value of  $-26$  nm [Figs. 9(b) and 9(c)].

In another area of the same boundary, several steps were present [Fig. 10(a)]. Four defects have been analyzed by mapping circuits drawn around them into the dichromatic pattern, they are summarized in Table IV. The Burgers vec-

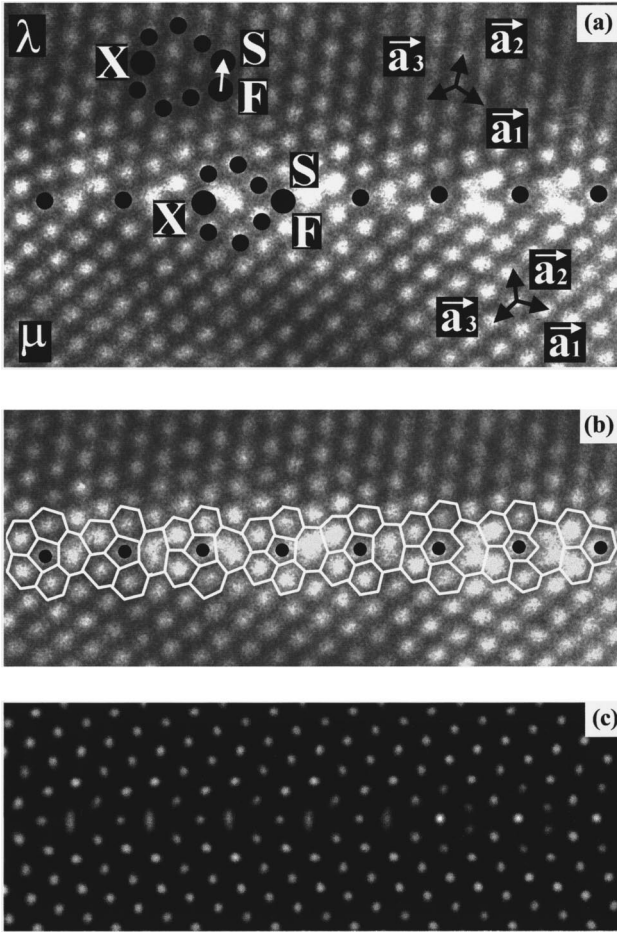


FIG. 9. The symmetric  $\Sigma=7:21.79^\circ/[0001]$  boundary: (a) The period is indicated by the largest black dots. (b) Reconstruction of the same grain boundary made of 5/7 and 8 atom rings. (c) Simulated image using the above reconstructed model at 5 nm thickness and  $-26$  nm defocus.

tors of the secondary dislocations correspond again to the smallest vectors of the dichromatic pattern (Fig. 8) with steps heights of 1 ( $\lambda$ ) and 2 ( $\mu$ ) planes, respectively: i.e.,  $b_{1/2} = 1/21 [\bar{1}5\bar{4}0]_\lambda$ .

Schematic illustrations of these defects are drawn with the translation vectors given in Table IV (Fig. 11) and compared to the experimental image. For defects numbered 1, 3, and 4, the reconstructions are consistent with the experimental image. However, for defect 2, whose Burgers vector is  $\mathbf{b}_{1/2} = 1/21 [\bar{1}5\bar{4}0]_\lambda$ , the value of the smallest crystal translation vectors implies re-entrant steps, as shown in Fig. 11(b). If a translation vector of the  $(\bar{2}3\bar{1}0)_\lambda$  interface, equal to  $1/3 [\bar{4}\bar{1}50]_\lambda$  is added to  $\mathbf{t}(\lambda)$  and  $\mathbf{t}(\mu)$ , the step configura-

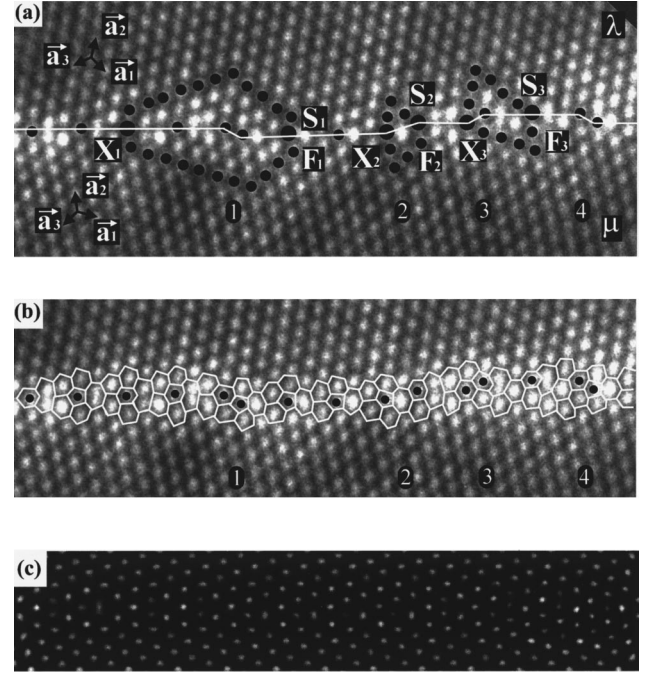


FIG. 10. Another part of the  $\Sigma=7$  grain boundary where steps are present: (a) Several circuits have been drawn in order to analyze the steps numbered from 1 to 4. (b) Reconstruction. (c) Simulated image of the boundary (thickness: 6 nm and defocus:  $-26$  nm).

tion illustrated in Fig. 11(c) becomes consistent with the image; it exhibits a larger step riser than the other defects.

Between the steps, the interface plane consists of primary dislocations and their cores were found to be made of 5/7- and 8-atom rings. As shown in Fig. 10(b), twelve primary dislocations are present, among which six correspond to the 8-atom rings and the six others exhibit 5/7-atom cycles, there is no regular distribution of these configurations along the interface. A simulated image corresponding to these configurations has been carried out [Fig. 10(c)]. A good agreement is obtained with the experimental image for a thickness of 6 nm and a defocus value of  $-26$  nm. Again this symmetric boundary exhibits structural units corresponding only to the cores of isolated  $\mathbf{a}$  edge dislocations of the bulk GaN.

### C. The $\Sigma=7$ asymmetric boundary

Another grain has been observed with a similar rotation angle of  $21.8^\circ$  and therefore corresponding to a  $\Sigma=7$  boundary. Contrary to the previous, it was characterized by large straight facets. Besides a symmetric interface similar to those previously studied, an asymmetric straight boundary was present as well. The interface plane was  $(\bar{3}8\bar{5}0)_\lambda / (01\bar{1}0)_\mu$  (Table V) and when mapped into the lattice of the  $\lambda$  crystal,

TABLE III. Determination of the  $\Sigma=7$  boundary plane by circuit mapping, SXF in Fig. 9(a).

$\lambda$ crystal	$\mu$ crystal	Defect/interface
$\mathbf{c}(\lambda) = \mathbf{S}\mathbf{X} = 1/3 [\bar{4}\bar{1}50]_\lambda$	$\mathbf{c}(\mu) = \mathbf{X}\mathbf{F} = 1/3 [5\bar{1}40]_\mu$	$\mathbf{c}(\lambda, \mu) = \mathbf{c}(\lambda) + P_7\mathbf{c}(\mu) = 0$
$\mathbf{n}_\lambda = \mathbf{c}(\lambda) \wedge [0001]$	$\mu = [0001] \wedge \mathbf{c}(\mu)$	$(\bar{2}3\bar{1}0)_\lambda / (\bar{1}3\bar{2}0)_\mu$
$= 1/3 [\bar{6}9\bar{3}0]_\lambda$	$= 1/3 [\bar{3}9\bar{6}0]_\mu$	

TABLE IV. Detailed analysis of the interfacial defects in the  $\Sigma=7$  boundary shown in Fig. 10(a).

	$\lambda$ crystal	$\mu$ crystal	Secondary dislocation
Defects 1 et 4	$\mathbf{c}(\lambda) = \mathbf{S}_1 \mathbf{X}_1 = 1/3 [14\bar{2} 16 0]_\lambda$ $h(\lambda) = -\mathbf{n}_\lambda \cdot \mathbf{c}(\lambda) = -2$ $\mathbf{t}(\lambda) = \bar{a}_1 = 1/3 [2\bar{1}\bar{1} 0]_\lambda$ $h(\lambda) = \mathbf{n}_\lambda \cdot \mathbf{t}(\lambda) = -2$	$\mathbf{c}(\mu) = \mathbf{X}_1 \mathbf{F}_1 = 1/3 [17 4\bar{13} 0]_\mu$ $h(\mu) = \mathbf{n}_\mu \cdot \mathbf{c}(\mu) = -1$ $\mathbf{t}(\mu) = \bar{a}_1 = 1/3 [2\bar{1}\bar{1} 0]_\mu$ $h(\mu) = \mathbf{n}_\mu \cdot \mathbf{t}(\mu) = -1$	$\mathbf{b}_{-2/-1} = -\mathbf{c}(\lambda, \mu) = -\mathbf{c}(\lambda) - P_7 \mathbf{c}(\mu)$ $= 1/21 [1\bar{5} 4 0]_\lambda$ $\mathbf{t}(\lambda) + P_7 \mathbf{t}(\mu) = 1/21 [1\bar{5} 4 0]_\lambda$
Defect 3	$\mathbf{c}(\lambda) = \mathbf{S}_3 \mathbf{X}_3 = 1/3 [5\bar{2} 7 0]_\lambda$ $h(\lambda) = -\mathbf{n}_\lambda \cdot \mathbf{c}(\lambda) = 1$ $\mathbf{t}(\lambda) = -\bar{a}_3 = 1/3 [1 1 \bar{2} 0]_\lambda$ $h(\lambda) = \mathbf{n}_\lambda \cdot \mathbf{t}(\lambda) = 1$	$\mathbf{c}(\mu) = \mathbf{X}_3 \mathbf{F}_3 = 1/3 [6 0 \bar{6} 0]_\mu$ $h(\mu) = \mathbf{n}_\mu \cdot \mathbf{c}(\mu) = 2$ $\mathbf{t}(\mu) = -\bar{a}_3 = 1/3 [1 1 \bar{2} 0]_\mu$ $h(\mu) = \mathbf{n}_\mu \cdot \mathbf{t}(\mu) = 2$	$\mathbf{b}_{1/2} = \mathbf{c}(\lambda, \mu) = \mathbf{c}(\lambda) - P_7 \mathbf{c}(\mu)$ $= 1/21 [5\bar{4} \bar{1} 0]_\lambda$ $\mathbf{t}(\lambda) + P_7 \mathbf{t}(\mu) = 1/21 [5\bar{4} \bar{1} 0]_\lambda$
Defect 2	$\mathbf{c}(\lambda) = \mathbf{S}_2 \mathbf{X}_2 = 1/3 [2\bar{2} 2 4 0]_\lambda$ $h(\lambda) = 2$ $\mathbf{t}(\lambda) = -\bar{a}_1 = 1/3 [2\bar{1} 1 0]_\lambda$ $h(\lambda) = 2$ $\mathbf{t}'(\lambda) = 1/3 [2 2 \bar{4} 0]_\lambda = \mathbf{X}_2 \mathbf{S}_2 =$ $-\mathbf{c}(\lambda)$	$\mathbf{c}(\mu) = \mathbf{X}_2 \mathbf{F}_2 = 1/3 [3 0 \bar{3} 0]_\mu$ $h(\mu) = 1$ $\mathbf{t}(\mu) = -\bar{a}_1 = 1/3 [2\bar{1} 1 0]_\mu$ $h(\mu) = 1$ $\mathbf{t}'(\mu) = 1/3 [3 0 \bar{3} 0]_\mu = \mathbf{X}_2 \mathbf{F}_2 =$ $\mathbf{c}(\mu)$	$\mathbf{b}_{2/1} = 1/21 [\bar{1} 5 \bar{4} 0]_\lambda$ , $\mathbf{t}(\lambda) + P_7 \mathbf{t}(\mu) = 1/21 [\bar{1} 5 \bar{4} 0]$ $\mathbf{t}'(\lambda) + P_7 \mathbf{t}'(\mu) = 1/21 [\bar{1} 5 \bar{4} 0]$

the circuit SXF [Fig. 12(a)] exhibits the closure failure  $\mathbf{FS} = 2\bar{a}_2 - \bar{a}_3$ . Meaning that the period for this boundary is made of three edge dislocations. For four periods, we have determined that no secondary dislocation was present (Table V).

The reconstruction of these periods needs the presence of one 4 cycle in a new configuration 5/4/7 atom rings. This new configuration forms a characteristic pattern that allowed to determine the different periods without ambiguity. In between, the other two primary dislocations exhibit 5/7- and 8-atom ring cycles [Fig. 12(b)]. A simulated image based on this reconstruction has been calculated and it agrees fairly well with the experimental HREM image [Fig. 12(c)].

A neighbor area of the boundary was studied and a step was present at the interface [Fig. 13(a)]. However, when the circuit  $S_1 X_3 F_1$  was mapped in the dichromatic pattern, no additional defect was found as  $\mathbf{c}(\lambda) + P_7 \mathbf{c}(\mu)$  was equal to zero (zone B in Table VI). In fact, the step is clearly visible between  $S_2$  and  $S_3$  and the study of the circuit  $S_2 S_3 F_2$  with  $\mathbf{c}'(\lambda) = \mathbf{S}_2 \mathbf{S}_3$  and  $\mathbf{c}'(\mu) = \mathbf{S}_3 \mathbf{F}_2$  indicates that the circuit  $S_2 S_3 F_2$  is a defect-free step. A closer examination shows that in this area, the interface plane is  $(\bar{2}3\bar{1}0)_\lambda / (\bar{1}3\bar{2}0)_\mu$ , which corresponds to a side of the CSL unit cell. This allows to shift the  $(\bar{3}8\bar{5}0)_\lambda / (01\bar{1}0)_\mu$  boundary plane without introducing an interfacial dislocation. In the periods labeled 1 and 4, the pattern composed of the 5/4/7-atom cycles is present and the two other dislocation cores are made of two 5/7-atom cycles for period 4 and one 8 and one 5/7 ones for period 1. The end and the beginning of the period 2 are the same as for period 4: two 5/7 atom cycles are present, but, the new configuration has been replaced by a configuration made of one 8 atom cycle. For period 3, which corresponds to a side of the CSL unit cell and is similar to the boundaries previously studied, the dislocation core is made of one 5/7-atom rings model. A good agreement is observed between the HREM experimental image and the simulation based on this reconstruction [Figs. 13(b) and 13(c)].

In another area, where no additional defect was detected even if a step was clearly visible, circuit mapping indicates that this defect-free step defines an interface plane  $(\bar{1}5\bar{4}0)_\lambda / (14\bar{5}0)_\mu$ , which corresponds to a diagonal of the CSL unit cell.

In this asymmetric  $\Sigma=7$  boundary, we have found a new structural unit in which the primary dislocations have a 5/4/7-atom ring configuration. Moreover, it is pointed out that the boundary can change plane by forming steps corresponding to a diagonal or side of the CSL, in that case, no interfacial defect is introduced by such steps.

#### D. The $\Sigma=31$ symmetric boundary

This grain boundary is very irregular and we discuss the analysis carried out on four periods (Fig. 14). The corre-

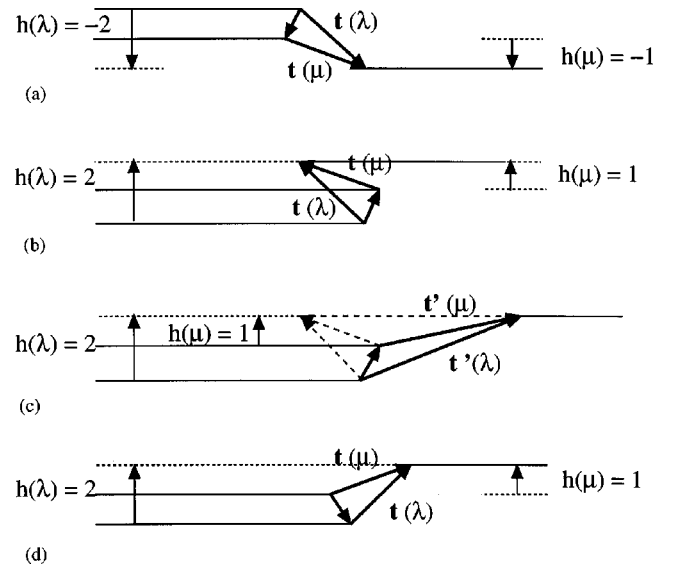


FIG. 11. Schematic illustration of the steps (a) Defects 1 and 4, (b) Defect 2 with a re-entrant step. (c) Arrangement in order to avoid the re-entrant step situation. (d) Defect 3.

TABLE V. Determination of interface plane and defect content in the  $\Sigma=7$  asymmetric boundary of Fig. 12(a).

$\lambda$ crystal	$\mu$ crystal	Interface
$\mathbf{c}(\lambda) = 1/3 [\bar{1}32\ 110]_{\lambda}$	$\mathbf{c}(\mu) = 1/3 [14\bar{7}\ \bar{7}0]_{\mu}$	$(\bar{3}\ 8\ \bar{5}\ 0)_{\lambda} / (0\ 1\ \bar{1}\ 0)_{\mu}$
$\mathbf{n}_{\lambda} = [\bar{3}\ 8\ \bar{5}\ 0]_{\lambda}$	$\mathbf{n}_{\mu} = [0\ 7\ \bar{7}\ 0]_{\mu}$	
$\mathbf{c}(\lambda) = 1/3 [\bar{5}2\ 8\ 440]_{\lambda}$	$\mathbf{c}(\mu) = 1/3 [56\ \bar{2}8\ \bar{2}80]_{\mu}$	$\mathbf{c}(\lambda) + P_7\mathbf{c}(\mu) = 0$

sponding diffraction pattern indicates a rotation angle equal to  $18^{\circ} \pm 0.2^{\circ}$ , close to that of  $\Sigma=31(17.90^{\circ})$ . The circuit SXF, drawn in period 1 [Fig. 14(a)] mapped in the  $\lambda$  and  $\mu$  crystals leads to the interface plane  $(\bar{7}11\bar{4}0)_{\lambda} / (\bar{4}11\bar{7}0)_{\mu}$  (Table VII). This corresponds to a diagonal of the CSL unit cell. When this circuit was reported in the  $\lambda$  lattice, the total Burgers vector of the period was found to be  $3\bar{a}_2$ . However, for period 3, when the circuit  $S_1X_1F_1$  is mapped into the dichromatic pattern, a secondary dislocation is detected with Burgers vector  $\mathbf{b}_{-4/-7} = 1/31 [\bar{6}510]_{\lambda}$ . The corresponding shortest translation vectors are  $\mathbf{t}(\lambda) = \bar{a}_3$  and  $\mathbf{t}(\mu) = -\bar{a}_3$ , consistent with the values of step heights and Burgers vector, except for the sign of the vectors which implies re-entrant steps. However, if a translation vector of the  $[\bar{7}11\bar{4}0]_{\lambda}$  interface, that is  $[51\bar{6}0]_{\lambda}$  is added to  $\mathbf{t}(\lambda)$  and  $\mathbf{t}(\mu)$ , the step configuration agrees well with the experimental image.

In this micrograph, four periods are present and they all exhibit three dislocation cores even the one which presents a defect character [Fig. 14(b)]. A simulated image [Fig. 14(c)] using this reconstruction agrees fairly well with the experimental image. The three primary dislocations of each period are regularly spaced. Their cores are mainly reconstructed with the 5/7 and 8 structural units. However, the most interesting finding is the occurrence of the 4 atom cycle in period 2. Unlike the previous case of the asymmetric  $\Sigma=7$  boundary in which such cycles were always inserted between 5 and 7-atom rings, this one is similar to the model deduced from anisotropic elasticity calculations and it forms an individual primary dislocation of the grain boundary.

## VI. DISCUSSION AND CONCLUSION

Due to the mosaic structure of the layers, numerous edge dislocations are present with very high densities

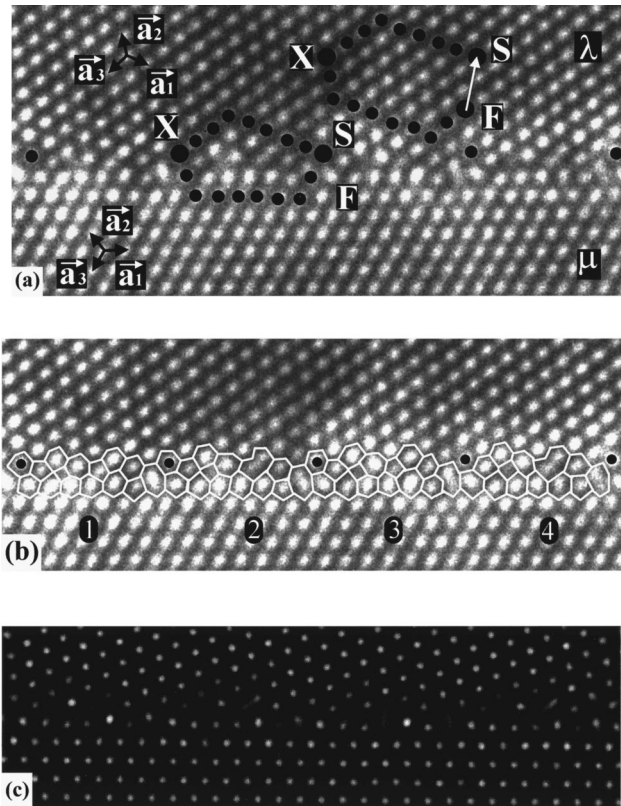


FIG. 12. Asymmetric  $\Sigma=7$   $(\bar{3}8\bar{5}0)_{\lambda} / (01\bar{1}0)_{\mu}$  grain boundary: (a) Mapped circuits and determination of the periods in the boundary as indicated by the large black dots. (b) Reconstruction of the boundary made of 5/7, 8, and 5/4/7 atom cycles. (c) Corresponding simulation (thickness: 6 nm and defocus:  $-26$  nm).

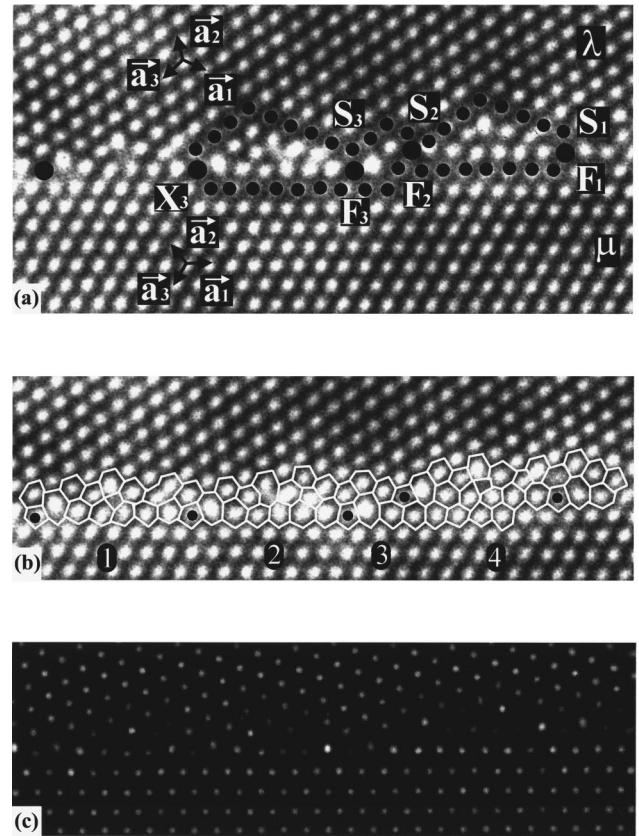


FIG. 13. An area of the asymmetric  $\Sigma=7$   $(\bar{3}8\bar{5}0)_{\lambda} / (01\bar{1}0)_{\mu}$  boundary (zone B in Table VI) (a) A defect-free step  $S_2S_3F_2$  is present. (b) Reconstruction. (c) Simulated image of the boundary (thickness: 6 nm and defocus:  $-26$  nm).

TABLE VI. Defect free steps in a  $\Sigma=7$  asymmetric boundary of Fig. 13(a).

	$\lambda$ crystal	$\mu$ crystal	Interface
zone B	$\mathbf{c}(\lambda) = \mathbf{S}_1 \mathbf{X}_3 = 1/3[\overline{30} 3 27 0]_\lambda$	$\mathbf{c}(\mu) = \mathbf{X}_3 \mathbf{F}_1 = 1/3[33 \overline{15} \overline{18} 0]_\mu$	$\mathbf{c}(\lambda) + P7 \mathbf{c}(\mu) = 0$
	$\mathbf{c}'(\lambda) = \mathbf{S}_2 \mathbf{S}_3 = 1/3[\overline{4} \overline{1} 5 0]_\lambda$	$\mathbf{c}'(\mu) = \mathbf{S}_3 \mathbf{F}_2 = 1/3 [5 \overline{1} 4 0]_\mu$	$(\overline{2} 3 \overline{1} 0)_\lambda / (\overline{1} 3 \overline{2} 0)_\mu$
zone C	$\mathbf{n}_\lambda = 1/3 [\overline{2} 3 \overline{1} 0]_\lambda$	$\mathbf{n}_\mu = 1/3 [\overline{1} 3 \overline{2} 0]_\mu$	
	$\mathbf{c}(\lambda) = \mathbf{S}_2 \mathbf{S}_3 = [\overline{3} 1 2 0]_\lambda$	$\mathbf{c}(\mu) = \mathbf{S}_3 \mathbf{F}_2 = [\overline{3} \overline{2} \overline{1} 0]$	$(\overline{1} 5 \overline{4} 0)_\lambda / (14 \overline{5} 0)_\mu$
	$\mathbf{n}_\lambda = 1/3 [\overline{1} 5 \overline{4} 0]_\lambda$	$\mathbf{n}_\mu = 1/3 [1 4 \overline{5} 0]_\mu$	

( $10^{10} \text{ cm}^{-2}$ ); they form low-angle grain boundaries that are rotated about the  $\mathbf{c}$  axis. As the rotation angles are small ( $< 1^\circ$ ), the distance between the dislocations is quite large  $\geq 100$  nm. Early work on the mosaic growth explained these large densities by assuming that the small rotations around the  $c$  axis were due to growth errors.<sup>2</sup> Later observations have shown that, whereas the conventional epitaxial relationship  $(0001)_{\text{GaN}}(0001)_{\text{sapphire}}$ ,  $[11\overline{2}0]_{\text{GaN}}/[\overline{1}0\overline{1}0]_{\text{sapphire}}$  was predominant, at least inside the buffer layer, other orientations of grains have been reported<sup>4,5</sup> and shown to exhibit a smaller mismatch (1.5%) than that in the usual growth.<sup>4</sup> The high-angle grain boundaries observed in this work were found to extend from the GaN/sapphire interface to the GaN film surface. In the layers, the density of threading dislocations is not unusually high ( $10^{10} \text{ cm}^{-2}$ ). It is therefore possible that the mosaic growth of GaN on top of (0001) sapphire does not only include the small angle rotations between adjacent grains, which are due to growth errors, but also local arrangements of the threading dislocations into high-angle grain boundaries.

This high-resolution electron microscopy analysis presents evidence of multiple core structure for the  $\vec{a}$  pure-edge dislocation in GaN layers. Our observations show that mainly two atomic configurations are present with 5/7- and 8-atom cycles at a similar frequency in low-angle boundaries. For the 5/7-atom cycle configuration, it is interesting to note that a Ga-Ga core would present different properties to a N-N configuration.

The topological theory formalism, which comprises the crystallographic analysis with dichromatic patterns and circuit mapping has been used to characterize the interface structure of three different CSL tilt grains about [0001]. This has allowed us to completely determine the nature of the boundary planes and the various step risers, which were found to have or not a defect character. The Burgers vectors of the primary dislocations have been found to correspond to  $\vec{a}$  pure-edge dislocations with the 5/7- and 8-atom ring cores. In some of the boundaries, we have pointed out the occurrence of the 4-atom ring cores, with the formation of a more complicated configuration, 5/4/7-atom rings in asymmetric boundaries.

The interfacial defects, which lead to deviation of the boundaries from coincidence, have been determined. In all the cases their Burgers vectors correspond to the smallest vector of the DSC as measured in the dichromatic patterns.

## APPENDIX

The transformation  $P$  matrices from the  $\mu$  to  $\lambda$  crystals depend on the rotation axis and angle. We have calculated

them for the three types of boundaries using the method proposed by Pond *et al.*<sup>27</sup> where the symmetry operations such as mirrors and rotations are expressed in the 4 coordinate frame of Frank.<sup>26</sup> The matrix  $R$  that represents a rotation through an angle  $\theta$  about the [0001] axis is

$$R = \begin{bmatrix} \cos \theta & -\sin \theta & 0 & 0 \\ \sin \theta & \cos \theta & 0 & 0 \\ 0 & 0 & 1 & 0 \\ 0 & 0 & 0 & 1 \end{bmatrix}.$$

In the 4 coordinate frame,  $R$  has to be expressed as a rotation about an appropriate direction  $[u_3, v_3, t_3, \Lambda w_3]_4$  which belongs to the reference structure. Then the transformation matrix  $P$  is obtained by calculating  $TRT^{-1}$ , where  $T$  is:

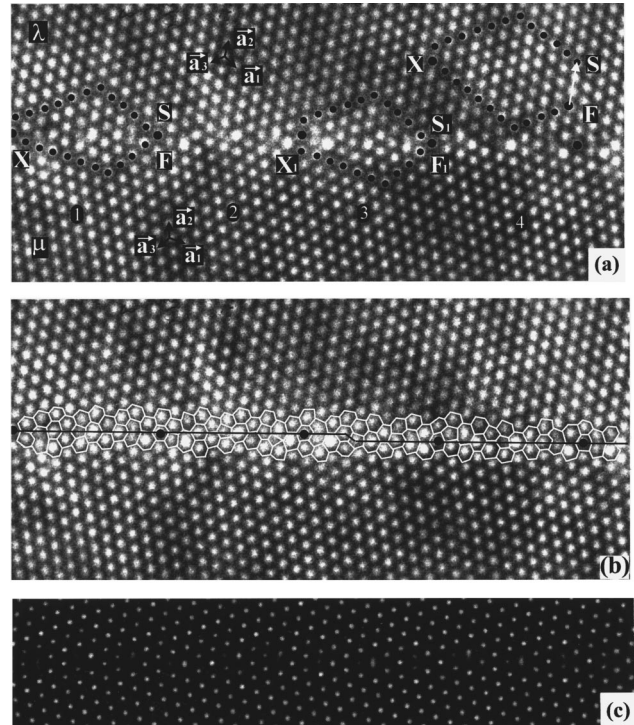


FIG. 14. High-resolution image of  $\Sigma=31$  grain boundary: (a) The large black dots define periods. (b) Reconstruction of the boundary, with a step inside the period 3. (c) Corresponding simulated image (thickness: 6 nm, defocus:  $-26$  nm).

TABLE VII. Determination of the defect content in the  $\Sigma = 31$  boundary area shown in Fig. 14(a), the interfacial dislocation  $\mathbf{b}_{-4/-7}$  has the smallest length in the dichromatic pattern.

$\lambda$ crystal	$\mu$ crystal	Interface
$\mathbf{c}(\lambda) = \mathbf{SX} = [\bar{5} \bar{1} 6 0]_\lambda$	$\mathbf{c}(\mu) = \mathbf{XF} = [6 \bar{1} \bar{5} 0]_\mu$	$(\bar{7} 11 \bar{4} 0)_\lambda / (\bar{4} 11 \bar{7} 0)_\mu$
$\mathbf{n}_\lambda = [\bar{7} 11 \bar{4} 0]_\lambda$	$\mathbf{n}_\mu = [\bar{4} 11 \bar{7} 0]_\mu$	
$\mathbf{c}(\lambda) = \mathbf{S}_1 \mathbf{X}_1 = 1/3 [\bar{14} \bar{2} 16 0]_\lambda$	$\mathbf{c}(\mu) = \mathbf{X}_1 \mathbf{F}_1 = 1/3 [17 \bar{4} \bar{13} 0]_\mu$	$\mathbf{c}(\lambda, \mu) = 1/31 [6 \bar{5} \bar{1} 0]_\lambda$
$h(\lambda) = -\mathbf{n}_\lambda \cdot \mathbf{c}(\lambda) = -4$	$h(\mu) = \mathbf{n}_\mu \cdot \mathbf{c}(\mu) = -7$	$\mathbf{b}_{-4/-7} = 1/31 [\bar{6} 5 1 0]_\lambda$
$\mathbf{t}(\lambda) = \bar{a}_3 = 1/3 [\bar{1} \bar{1} 2 0]_\lambda$	$\mathbf{t}(\mu) = -\bar{a}_3 = 1/3 [\bar{1} \bar{1} 2 0]_\mu$	
$\mathbf{t}'(\lambda) = 1/3 [14 2 \bar{16} 0]_\lambda = \mathbf{X}_1 \mathbf{X}_1 = -\mathbf{c}(\lambda)$	$\mathbf{t}'(\mu) = 1/3 [17 \bar{4} \bar{13} 0]_\mu = \mathbf{X}_1 \mathbf{F}_1 = \mathbf{c}(\mu)$	

$$T = \begin{bmatrix} u_1 & u_2 & u_3 & 1/\sqrt{3} \\ v_1 & v_2 & v_3 & 1/\sqrt{3} \\ t_1 & t_2 & t_3 & 1/\sqrt{3} \\ \Lambda w_1 & \Lambda w_2 & \Lambda w_3 & 0 \end{bmatrix}.$$

The column vectors of  $T$  are parallel to the axes of the initial system transformed to the Frank notation.  $[u_3, v_3, t_3, \Lambda w_3]_4$  is the rotation axis and the first two constitute an orthogonal basis system with it. The last vector  $1/\sqrt{3} [1110]_4$  is the unit vector along the projection direction as used by Frank in order to generate the usual 3 dimensional Miller-Bravais indices from his four dimensional space.

In the case of a rotation about the  $[0001]$  axis, these vectors are respectively parallel to  $[1\bar{1}00]_4$ ,  $[11\bar{2}0]_4$ ,  $[000\Lambda]_4$ , and  $[1110]_4$ ; therefore, the  $T$  matrix becomes

$$T = \begin{bmatrix} 1/\sqrt{2} & 1/\sqrt{6} & 0 & 1/\sqrt{3} \\ -1/\sqrt{2} & 1/\sqrt{6} & 0 & 1/\sqrt{3} \\ 0 & -2/\sqrt{6} & 0 & 1/\sqrt{3} \\ 0 & 0 & \Lambda & 0 \end{bmatrix}.$$

The general expression of  $P$  for such a rotation is:

$$P = TRT^1 = \begin{bmatrix} \frac{2}{3} \cos \theta + \frac{1}{3} & \frac{-1}{3} \cos \theta - \frac{1}{\sqrt{3}} \sin \theta + \frac{1}{3} & \frac{-1}{3} \cos \theta + \frac{1}{\sqrt{3}} \sin \theta + \frac{1}{3} & 0 \\ \frac{-1}{3} \cos \theta + \frac{1}{\sqrt{3}} \sin \theta + \frac{1}{3} & \frac{2}{3} \cos \theta + \frac{1}{3} & \frac{-1}{3} \cos \theta - \frac{1}{\sqrt{3}} \sin \theta + \frac{1}{3} & 0 \\ \frac{-1}{3} \cos \theta - \frac{1}{\sqrt{3}} \sin \theta + \frac{1}{3} & \frac{-1}{3} \cos \theta + \frac{1}{\sqrt{3}} \sin \theta + \frac{1}{3} & \frac{2}{3} \cos \theta + \frac{1}{3} & 0 \\ 0 & 0 & 0 & 1 \end{bmatrix},$$

which becomes for the rotations that we have investigated

$$\Sigma = 7, \theta = 21,79^\circ \quad P_7 = \frac{1}{21} \begin{bmatrix} 20 & \bar{4} & 5 & 0 \\ 5 & 20 & \bar{4} & 0 \\ \bar{4} & 5 & 20 & 0 \\ 0 & 0 & 0 & 21 \end{bmatrix}$$

$$\Sigma = 19, \theta = 13, 17^\circ \quad P_{19} = \frac{1}{57} \begin{bmatrix} 56 & \bar{7} & 8 & 0 \\ 8 & 56 & \bar{7} & 0 \\ \bar{7} & 8 & 56 & 0 \\ 0 & 0 & 0 & 57 \end{bmatrix}$$

$$\Sigma = 31, \theta = 17, 89^\circ \quad P_{31} = \frac{1}{31} \begin{bmatrix} 30 & \bar{5} & 6 & 0 \\ 6 & 30 & \bar{5} & 0 \\ \bar{5} & 6 & 30 & 0 \\ 0 & 0 & 0 & 31 \end{bmatrix}.$$

- \*Author to whom all correspondence should be addressed: FAX: 33 2 31 45 26 60. Electronic address: ruterana@lermat8.ismra.fr
- <sup>1</sup>S. Nakamura, M. Senoh, S. I. Nagahama, N. Iwaka, T. Yamada, T. Matsushita, and H. Kiyoku, *Jpn. J. Appl. Phys., Part 2* **74**, L35 (1996).
- <sup>2</sup>X. J. Ning, F. R. Chien, P. Pirouz, J. W. Wang, and M. A. Khan, *J. Mater. Res.* **3**, 580 (1996).
- <sup>3</sup>F. A. Ponce, *MRS Bull.* **22**, 51 (1997).
- <sup>4</sup>V. Potin, P. Ruterana, and G. Nouet, *Mater. Sci. Eng., B* **50**, 29 (1997).
- <sup>5</sup>N. Grandjean, J. Massies, P. Vennegues, M. Laugt, and M. Leroux, in *III-V nitrides*, edited by F. A. Ponce, T. D. Moustakas, I. Akasaki, and B. A. Monemar, *MRS Symposia Proceedings No. 449* (Materials Research Society, Pittsburgh, 1996), p. 67.
- <sup>6</sup>J. L. Rouvière, *Mater. Sci. Eng., B* **50**, 61 (1997).
- <sup>7</sup>J. Elsner, R. Jones, P. K. Sitch, V. D. Porezag, M. Elstner, T. Frauenheim, M. I. Heggie, S. Oberg, and P. R. Briddon, *Phys. Rev. Lett.* **79**, 3672 (1998).
- <sup>8</sup>Y. Xin, S. J. Pennycook, N. D. Browning, P. D. Nellist, S. Sivanathan, F. Omnès, B. Beaumont, J. P. Faurie, and P. Gibart, *Appl. Phys. Lett.* **72**, 2680 (1998).
- <sup>9</sup>L. W. Tu, Y. C. Lee, C. J. Chen, I. Lo, D. Stocker, and E. F. Schubert, *Appl. Phys. Lett.* **73**, 2802 (1998).
- <sup>10</sup>T. S. Zheleva, O. K. Nam, M. D. Bremser, and R. F. Davis, *Appl. Phys. Lett.* **71**, 2472 (1997).
- <sup>11</sup>P. Vennegues, B. Beaumont, S. Haffouz, M. Vaille, and P. Gibart, *J. Cryst. Growth* **189**, 97 (1998).
- <sup>12</sup>R. F. Davis, in *Microscopy of Semiconducting Materials 1999*, edited by A. G. Cullis and R. Beanland, *IOP Conf. Proc. (Institute of Physics, London, in press)*.
- <sup>13</sup>A. Bourret, J. Desseaux, and A. Renault, *Philos. Mag. A* **45**, 1 (1982).
- <sup>14</sup>V. Vitek, A. P. Sutton, G. J. Wang, and D. Schwartz, *Scr. Metall.* **17**, 183 (1983).
- <sup>15</sup>W. Bollmann, *Crystal Defects and Crystalline Interfaces* (Springer-Verlag, Berlin, 1970).
- <sup>16</sup>F. R. Chen and A. King, *Philos. Mag. A* **57**, 431 (1988).
- <sup>17</sup>I. McLaren and M. Aindow, *Scr. Metall.* **29**, 811 (1993).
- <sup>18</sup>A. P. Sutton, *Philos. Mag. Lett.* **59**, 53 (1989).
- <sup>19</sup>R. Portier, D. Gratias, and M. Fayard, *Acta Crystallogr., Sect. A: Cryst. Phys., Diff., Theor. Gen. Crystallogr.* **35**, 885 (1979).
- <sup>20</sup>R. C. Pond and D. S. Vlachavas, *Proc. R. Soc. London, Ser. A* **386**, 95 (1983).
- <sup>21</sup>R. C. Pond, *Interface Sci.* **2**, 1 (1995).
- <sup>22</sup>A. P. Sutton and R. W. Balluffi, *Interfaces in Crystalline Materials* (Clarendon, Oxford, 1995).
- <sup>23</sup>F. Sarrazit, R. C. Pond, and N. A. Kiselev, *Philos. Mag. Lett.* **77**, 191 (1998).
- <sup>24</sup>*International Tables for Crystallography*, edited by T. Hahn (Kluwer Academic, Dordrecht, The Netherlands, 1996), Vol. A, p. 590.
- <sup>25</sup>P. Vermaut, P. Ruterana, and G. Nouet, *Philos. Mag. A* **76**, 1215 (1997).
- <sup>26</sup>R. C. Pond, in *Dislocations in Solids*, edited by F. R. N. Nabarro (North-Holland, Amsterdam, 1989), Vol. 8, p. 1.
- <sup>27</sup>F. C. Frank, *Acta Crystallogr.* **18**, 862 (1965).
- <sup>28</sup>R. C. Pond, N. A. Mc Auley, A. Serra, and W. A. T. Clark, *Scr. Metall.* **21**, 197 (1987).
- <sup>29</sup>J. P. Hirth and R. C. Pond, *Acta Mater.* **44**, 4749 (1996).
- <sup>30</sup>T. Braisaz, P. Ruterana, G. Nouet, and R. C. Pond, *Mater. Sci. Forum* **207**, 113 (1996).
- <sup>31</sup>T. Braisaz, P. Ruterana, G. Nouet, and R. C. Pond, *Philos. Mag. A* **75**, 1075 (1997).
- <sup>32</sup>A. Serra and D. J. Bacon, *Philos. Mag. A* **73**, 333 (1996).
- <sup>33</sup>R. Bonnet, *Acta Metall.* **29**, 437 (1981).
- <sup>34</sup>P. A. Stadelmann, *Ultramicroscopy* **21**, 131 (1987).
- <sup>35</sup>V. Potin, P. Ruterana, A. Hairie, and G. Nouet, in *Nitride Semiconductors*, edited by F. A. Ponce, S. P. Denbaars, B. K. Meyers, S. Nakamura, and S. Strite, *MRS Symposia Proceedings No. 482* (Materials Research Society, Pittsburgh, 1998), p. 435.
- <sup>36</sup>P. Vermaut, P. Ruterana, G. Nouet, and H. Morkoç, in *Microscopy of Semiconducting Materials 1995*, edited by A. G. Cullis and A. E. Staton-Bevan, *IOP Conf. Proc. No. 146* (Institute of Physics, London, 1995), p. 289.
- <sup>37</sup>J. Hornstra, *J. Phys. Chem. Solids* **5**, 129 (1957).
- <sup>38</sup>A. M. Papon and M. Petit, *Scr. Metall.* **19**, 391 (1985).
- <sup>39</sup>A. Vila, A. Cornet, J. R. Morante, P. Ruterana, M. Loubradou, R. Bonnet, Y. Gonzalez, and L. Gonzalez, *Philos. Mag. A* **71**, 85 (1995).
- <sup>40</sup>P. Vermaut, P. Ruterana, G. Nouet, and H. Morkoç, *Philos. Mag. A* **75**, 239 (1997).
- <sup>41</sup>P. Ruterana, B. Barbaray, A. Béré, G. Nouet, A. Hairie, E. Paumier, A. Salvador, A. Botchkarev, and H. Morkoç, *Phys. Rev. B* **59**, 15 917 (1999).